

Minute-Scale Wind Vector Forecasting Using Scanning Lidar Inputs to a Convolutional LSTM Neural Network

Elliot Simon and Michael Courtney

Technical University of Denmark, Department of Wind Energy (Risø Campus). Roskilde, Denmark

Correspondence: Elliot Simon <ellsim@dtu.dk>

Abstract.

The increasing share of wind power in energy systems leads to integration challenges for real time grid balancing and electricity market participation. As energy services move towards faster decision-action timeframes, improving the accuracy of wind power forecasts becomes crucial for ensuring system reliability and stable pricing. Forecasts on the minute-scale are traditionally based on statistical approaches using historical data. Remote sensing instruments such as pulsed scanning Doppler lidars are able to measure at long distances upwind of a wind turbine or wind farm and provide a preview of the approaching wind resource. Recent developments in machine learning have produced a convolutional-recurrent neural network unit called ConvLSTM. This enables models to learn from spatiotemporal patterns present in 2-Dimensional image sequences and use them to predict future outcomes.

- 5 To explore the possibilities of lidar-based wind forecasting, an artificial neural network (ANN) has been developed which utilizes lidar scans of the upstream horizontal wind field to predict downstream horizontal wind vectors in a multi-output fashion up to 5-minutes ahead. The results of the ANN-lidar model have been benchmarked against three common statistical approaches (persistence, AR, and ARIMA). The ANN-lidar approach has demonstrated skill below the 4-minute horizon, but has also highlighted challenges towards advancing the state of the art.
- 10
- 15

1 Introduction

1.1 Minute-scale forecasting of winds

Meteorological forecasts with time resolutions on the minute-scale are becoming increasingly useful in the wind energy field. The underlying variability of the wind resource, together with constraints from the power system and energy markets drives a need for accurate site-specific forecasts of impending conditions, particularly at large wind power plants. To date, the state 20 of the art for producing such forecasts is normally based on time series modelling of past observational data (Giebel et al. (2011)). Another advanced approach is to adapt the output from previously computed ensemble numerical weather prediction

(NWP) models to real-time measurements (Moehrle (2004)). The inclusion of local measurements in this manner has shown potential towards improving the inability of NWP models to correctly predict the timing, magnitude and duration of wind ramps- that is, large and sudden changes in the extractable energy in the wind (Mahoney et al. (2012)). However, in light of these developments, the most widely used technique by the wind power industry on timescales below 1-hour remains the
5 persistence method.

Persistence assumes that short-run future conditions will remain unchanged from the recent past. Due to the high temporal autocorrelation of winds on very-short timescales, this method has performed acceptably well to date. Yet by design, the persistence method fails to predict changes (such as weather fronts and ramp events) which results in undesired discrepancies in expected and actual production, as well as imperfect information being fed to control systems.

- 10 As energy systems across the world transition to higher shares of variable renewable generation, these forecast errors become increasingly problematic for maintaining stable frequency control and limiting financial risk for imbalances in the energy markets. Owners of wind power assets have historically been supported by agreements such as the feed-in-tariff (FIT) or other power purchase agreements (PPA) which disregard the timing of their production. As these programmes phase out, operators will face financial consequences for forecast errors as balance responsible parties (BRP).
- 15 To date, a number of national and regional grid operators support trading of energy in markets with delivery times on the minute-scale (EPEX SPOT (2019)), with others expected to follow suit as their share of renewable generation increases. Minute-scale wind forecasts are also an integral component of wind turbine and farm control applications, which aims to maximize energy production while minimizing fatigue and extreme loading of the structures.

1.2 Remote sensing of winds

- 20 With the advent of remote sensing technologies, it is now possible to measure winds at a distance, without the expense and limitations of tower based in situ sensors. Lidar technology in particular has benefitted from rapid cost decreases partly due to hardware overlaps with optical fiber components used in the telecommunications industry. Doppler wind lidars have found applicability in wind energy and proven their practicality within areas including: wind resource assessment (Brower (2012)), power performance verification (Wagner et al. (2014)), independent sensor (Ahsbahs et al. (2017)) and model (Veiga Rodrigues
25 et al. (2016), Mann et al. (2018), Vollmer et al. (2015)) validation, NWP data assimilation, operational turbine control (Schlipf et al. (2012)), among others.

In this paper we will solely refer to coherent pulsed scanning Doppler lidar technology. These instruments are active remote sensing devices which use shaped pulses of laser light, typically with a wavelength of 1.54 μm to probe the atmosphere. This wavelength was chosen as it corresponds to the absorption line of atmospheric water vapour and CO₂, meets eye safety
30 standards, and is compatible with hardware components developed in the telecom industry (Cariou et al. (2006)). Laser pulses are emitted in a collimated beam from the lidar's telescope which backscatter off of aerosols (particles suspended in the air) and in turn shift their frequency according to the Doppler principle. A small portion of the backscattered pulses are received by the

lidar's optical chain and through spectral processing a radial velocity is obtained. This radial velocity represents the projection of the wind velocity along the beam angle (line-of-sight, LOS). As pulsed lidars do not focus their beam, measurements at multiple distances (range gates, RG) are taken simultaneously. The values are calculated by range weighting of the spectra and discerned through a time-of-flight calculation based on the fixed speed of light. It is important to note that the lidars do not
5 measure at discrete points in space, but rather a volume-average of the backscattered pulses.

Scanning lidars are equipped with a movable scanner head with two degrees of freedom used to steer the beam along a given trajectory. This is achieved through control of the system's azimuth and elevation motors, while range gating accounts for the third degree of freedom. These capabilities allow for measuring in 1D (staring), 2D (plane), and 3D (volumetric) modes. In this study, we will employ the following two scan types:

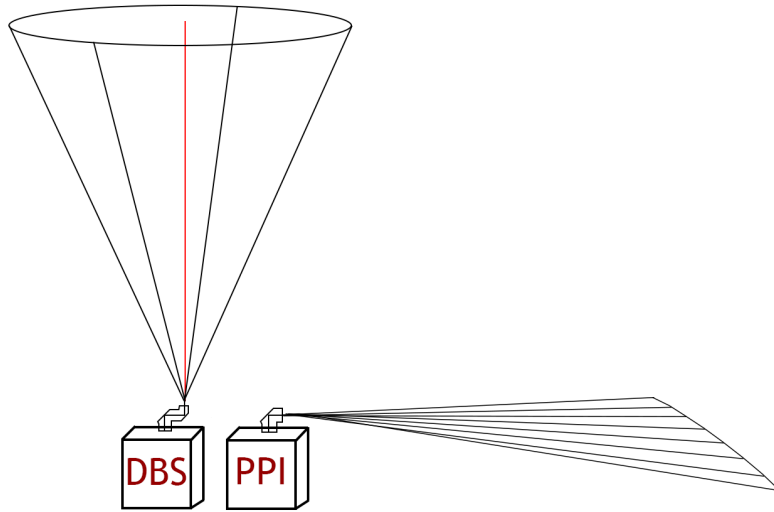


Figure 1. Depiction of Doppler beam swinging (DBS, left) and plan position indicator (PPI, right) scanning trajectories

- 10 – Doppler beam swinging (DBS) scans. Skyward facing DBS scans are used to measure the vertical wind profile by sampling at normally four orthogonal directions in addition to a vertical beam (Strauch et al. (1987)). Under the assumption of horizontal homogeneity and sampling concurrency, the horizontal wind vector is deduced with the vertical component being directly measured.
- 15 – Plan position indicator (PPI) scans. PPI scans are conducted by sweeping across a range of azimuths while holding the elevation angle constant. At zero degrees elevation this follows an arced horizontal plane representing a cross-section of horizontal winds projected along the azimuth of each beam direction.

Traditionally, radial velocity measurements from PPI scans are used to obtain horizontal wind vectors through single-Doppler velocity retrieval (SDVR) techniques such as the integrating Velocity Azimuth Process (IVAP) (Liang (2007)). This method

treats the line-of-sight measurements as different perspectives of the same homogeneous wind which reduces the data dimensionality to a time series of the horizontal wind components (u,v) at each range gate.

Wind patterns are discernable in the 2D scans themselves and contain spatial information which is largely lost using the classic SDVR techniques. By treating the PPI scans as a 2-dimensional image, we are able to employ techniques from the fields of
5 image processing and computer vision to make use of the spatial patterns contained within the scan. This is the chosen direction of this study.

1.3 Concept of lidar based forecasting

Remotely measured wind fields present the potential for improving these very-short term forecasts by integrating wind patterns measured upwind of a wind turbine or wind farm's position into a prediction model. The observed winds advect to some
10 degree downstream and the motion of coherent structures such as gusts, weather fronts, and turbulent eddies can provide forward looking information about conditions which arrive in the order of minutes ahead.

Pulsed scanning Doppler lidars are well suited for this application due to their high spatial and temporal resolution, extended field of vision (up to 10 km (Leosphere (2018)), 12 km (Halo Photonics (2018)) or 30 km (Mitsubishi Electric (2018))), configurable scan patterns, and ability to measure throughout diverse environmental conditions.

15 A number of studies have been conducted to date concerning forecasting for wind energy purposes using lidar observations directly. Carpenter (2013) demonstrates an advection based method which propagates wind fields of a site-specific ramp phenomenon downstream to produce a forecast up to 45 minutes ahead which significantly improved upon persistence while achieving peak performance at the 10 minute ahead forecast horizon. Magerman (2014) tracks spatial variances of turbulence and extractable energy content in the upstream wind to produce a wind power forecast several minutes ahead, and also tracks a
20 ramp event occurring due to a frontal passage over a one hour timescale. Valldecabres et al. (2017) demonstrates a lidar based advection approach to generate 5-minute ahead wind speeds of near-coastal flow. Another work by Valldecabres et al. (2018) applies a similar advection based methodology to dual Doppler radar measurements for producing probabilistic wind power forecasts up to 5-minutes ahead. A recent work by Simon et al. (2018) utilizes horizontally scanning lidars mounted alongside a met-mast to make wind speed predictions up to 1-hour ahead.

25 1.4 Artificial neural networks (ANN)

Artificial neural networks (ANNs) are computing systems which take inspiration from the structure of the cerebral cortex. That is, they are designed to simulate the way the human brain processes and analyzes information. ANNs are capable of both self-learning and generalization, and have demonstrated their prowess for modelling complex non-linear relationships (Ogunmolu et al. (2016)). Core applications of this technology include natural language processing (Kim (2014)), pattern recognition
30 (Taigman et al. (2014)), and sequence prediction (i.e. forecasting) (Laptev et al. (2017)). Supervised learning tasks use labelled

training data (known inputs and outputs) to refine model weights through the forward activation of outputs and the backwards propagation of errors. Once a model is fit to a set of known observations, it can then be used as an analytical tool for predicting out-of-sample data.

Recommended background readings for further general context in the field include Goodfellow et al. (2016), Google Developers (2019) and Li (2018).

The tracking of wind patterns from real-time 2D lidar scans applied as a forward prediction engine represents a spatiotemporal sequence forecasting problem. There are two classes of neural networks which are relevant for different elements of this application. Convolutional neural networks (CNN) apply a sliding kernel to an input image, which extracts features from the image while preserving the spatial relationships. CNNs are widely applied to computer vision and object tracking tasks, and 10 use a feed-forward architecture which only allows signals to travel in one direction (input to output). The second class are recurrent neural networks (RNNs), which in contrast to feed-forward designs, include loops to allow signals to travel in both directions of the network. Computations from past inputs are fed back into the network which imparts the ability for memory of sequences of inputs. As time series signals contain a high degree of temporal autocorrelation, RNNs are routinely applied to forecasting tasks. Today's state of the art RNNs mainly comprise of long short-term memory (LSTM) units (Hochreiter and 15 Schmidhuber (1997)) which were designed to use gating rather than activation functions to avoid the vanishing or exploding gradient problem (Greff et al. (2017)).

Shi et al. (2015) has introduced a combination of both classes which aims to capture spatiotemporal correlations by designing a model where the input-to-state and state-to-state transitions are convolutional (i.e. the input and recurrent transformations). The ConvLSTM unit is well suited for problems where both the spatial features and their correlations in time are fundamental 20 features of the phenomenon. In the seminal work, Shi et al. applied the ConvLSTM approach to precipitation nowcasting using radar reflectivity images as inputs which significantly outperforms fully connected (FC) LSTMs. The ConvLSTM units will similarly be applied here using the Doppler lidar scans together with pooling layers to extract the dominant features.

2 Motivations and research questions

The following questions represent the core aims that this research work sets out to answer:

- 25
- How do 2-dimensional lidar scans correlate to each other? Can the advection of winds be tracked?
 - Can 2D lidar scans be utilized as images in a convolutional LSTM neural network for generating minute-scale predictions?
 - Can such a model forecast wind vectors at a reference position minutes ahead with higher skill than relevant benchmark methods?

- Can this be accomplished in real-time so that the predictions can be put to practical use?

3 Field experiment

3.1 Site description

The field experiment for this study took place at the Risø Campus of the Technical University of Denmark, situated at the following coordinates: 55° 41' 21.2604" N latitude, 12° 6' 1.6632" E longitude. The site is located along the shore of Roskilde fjord, a predominately shallow inland body of water containing a number of small islands (see Fig. 2). Winds are measured both over land and water. The onshore topography is characterized by mostly flat terrain rising upwards from the shoreline at an average slope of 5 degrees. Onshore background surface roughness is estimated at 0.05 m. Trees and shelter belts exist nearby, along with small patches of forest. The small low-lying island wholly included in the measurement area is Elleore, a self-proclaimed independent Kingdom (Mislan and Streich (2019)). The western bank of the water is the peninsula Bognæs, a mainly forested area used for hunting and recreation.

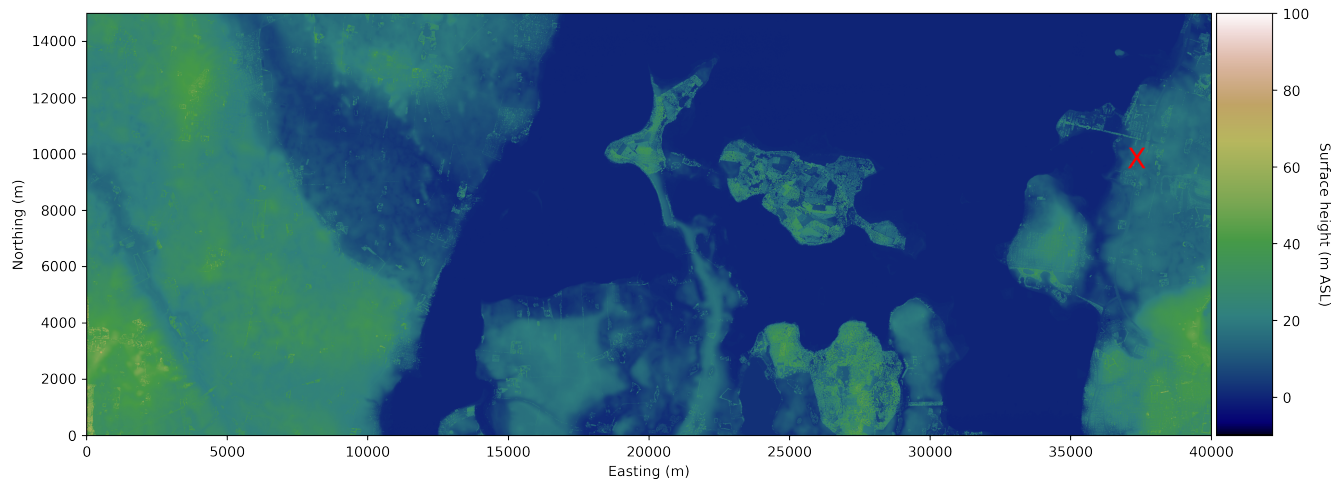


Figure 2. Digital surface model of the surrounding area. The lidar deployment area is denoted with a red X. Heights are relative to mean sea level

3.2 Measurement characteristics, configuration and pre-processing

3.2.1 Experiment overview

A field experiment involving a total of six scanning wind lidars was conducted during the autumn and winter of 2017-18 (October 12, 2017 – February 27, 2018). The goal of the experiment (designated LASCAR) was to obtain detailed measurements of the wind particularly for westerly inflows which develop over Roskilde fjord. Observations were made across flat horizontal and vertical planes, together with vertical profiles of the horizontal winds. In this study, we utilize data from two of the lidar systems deployed in the experiment.

All lidar instruments are of the DTU Long-Range WindScanner variety (Vasiljevic et al. (2016)). Key parameters of the measurement scenario are presented in Table 1 and Table 2 for each scanner respectively.

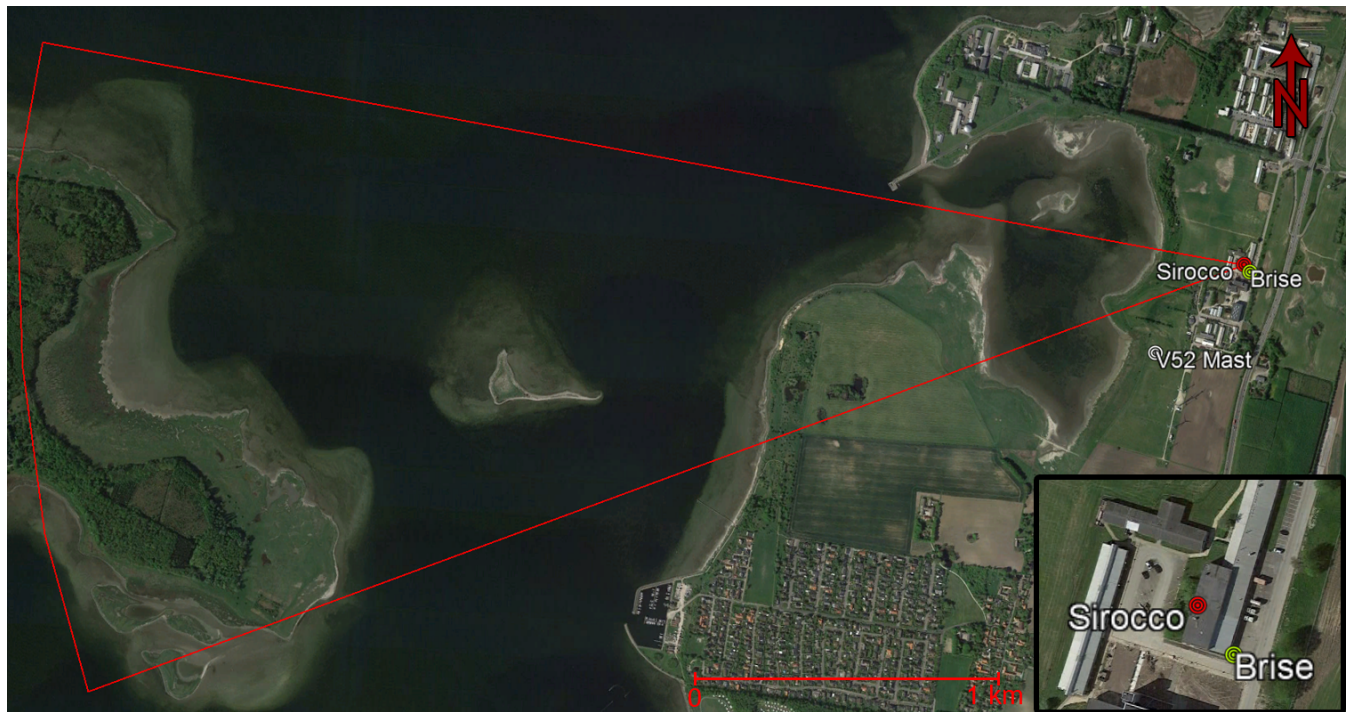


Figure 3. LASCAR experiment overview, with positions of the two scanning lidars and the met-mast denoted. The radius of the arc is 4 km

10 3.2.2 Sirocco unit – Plan position indicator (PPI)

In order to measure winds at the same height across all distances, the Sirocco unit was raised above ground with its elevation axis set to zero degrees. The lidar was deployed on the rooftop of Risø building 313, as shown in Fig. 3. This was accomplished

Table 1. Lidar specifications for the ‘Sirocco’ unit

Pulse length	200 ns (middle pulse)
Pulse energy	50 µJ
Pulse repetition frequency (PRF)	20 kHz
Probe length (FWHM)	35 m
Scan type	Plan position indicator (PPI)
Azimuth angle range	250 ° - 280 ° (30 ° sector size)
Elevation angle	0 °
Accumulation time	400 ms
FFT size	64 bins
Measurement range	80 – 4000 m
Range gate (RG) spacing	20 m (197 RGs)
Scanner head motion	2.5° / s
Reversing?	No. Scanner head resets to initial position following each scan
Number of lines-of-sight (LOS)	30 (1° LOS spacing)
Scan rate	13 s / scan (including reversing)

using a crane truck which lifted the device from the ground onto the roof, which was then carried manually into its position at the edge of the flat rooftop. The lidar’s height above mean-sea-level (AMSL) was measured at 22.07 m using a Leica Geosystems CS15 field controller and GS15 GPS receiver which has a 15 mm vertical static root-mean-square (RMS) accuracy (Leica Geosystems (2012)). Several points at the base of the building and coastline were also measured, leading to a determined height above ground-level (AGL) of 8.53 m and height above water-level (AWL) of 20.65 m at the time of measurement during typical conditions. The water level is subject to change, particularly during storms and under presiding northerly winds when water is transported into the fjord.

The system was levelled along both axes of the telescope using a digital level along with the system’s internal inclinometer. Standard procedures were followed to map multiple objects (hard targets) spaced across a range of positions in order to perform a static pointing calibration. Once the system’s position and orientation were known, offsets were hardcoded into the motion controller such that the zero degrees azimuth reference matched to north.

The lidar was configured according to Table 1 and set to perform repeating PPI scans as depicted with the red outline in Fig. 3. This entails keeping the elevation angle fixed while scanning over a range of azimuths to produce an arc slice through the horizontal wind.

Table 2. Lidar specifications for the ‘Brise’ unit

Pulse length	100 ns (short pulse)
Pulse energy	25 µJ
Pulse repetition frequency (PRF)	40 kHz
Probe length (FWHM)	25 m
Scan type	Doppler beam swinging (DBS)
Number of lines-of-sight (LOS)	5 beam method
Half cone angle	15 °
Accumulation time	1 s
FFT size	64 point
Measurement range	50 – 1000 m
Range gate (RG) spacing	10 m (96 RGs)
Scan rate	15 s / scan

3.2.3 Brise unit – Doppler beam swinging (DBS)

The Brise unit was deployed at ground level in the lee of the same building as Sirocco. Using the Leica controller, the height of Brise relative to Sirocco was found to be -7.8 m with a total Pythagorean distance between the two system’s telescopes equaling 31.86 m. The relative height difference differs from Sirocco’s height AGL as the terrain slopes down around the building. The 5 same levelling and calibration procedures were performed on Brise as Sirocco. The lidar was configured according to Table 2 and set to perform repeating DBS scans. This entails measuring along 4 fixed positions along a cone, followed by a central vertical beam which provides a direct measure of the vertical wind component.

3.2.4 Other instrumentation

Conventional (in situ) measurements from a nearby meteorological mast are used as an independent reference for validation 10 purposes. The source of the data is the meteorological mast 400 m directly southwest of the lidar deployment location (indicated in Fig. 3). The mast is an IEC compliant reference for DTU’s Vestas V52 research turbine. Ultrasonic anemometer measurements from 44 m AGL are used, as this is the closest instrumented height to Brise’s 50 m AGL range gate.

3.3 Data filtering and processing

A 12-hour continuous subset of the experiment has been selected for this study. Measurements obtained between November 15 14th at 16:45 and November 15th at 04:45 represent a population size of 3270 13-second samples (corresponding to the lidar’s

scan rate). The criteria used for selecting this period was for both lidar systems to be operational and the winds to originate broadly from the west (inflow to the experimental setup).

3.3.1 Sirocco unit (PPI scans)

A flowchart overview of the data processing steps for Sirocco is presented in Fig. 5.

- 5 Processing of the PPI scans from Sirocco began with reading in the radial speed measurements produced by the lidar system from all scenarios within the given time period. Timestamps were parsed from LabVIEW epoch time into datetime objects, with time zone conversion from UTC to local time (Central European Time, or UTC+1) in order to match the met-mast data logger convention.

Filtering steps included the removal of partial scans which can exist at the partition between scenario files. A carrier to noise ratio (CNR) threshold filter was applied which discarded measurements below -26 dB (low signal quality) and above 0 dB (hard target contamination). A radial speed filter was then applied which ensures that only periods of inflow, when the wind direction was approaching the lidar were considered. Next, a line-of-sight (LOS) filter was applied to reduce the angular width of scan from 30° to 21°. This was required as the azimuth range between 250° and 258° was contaminated by turbulence generated by a small patch of wooded trees. Finally, a range gate (RG) filter was applied which reduced the maximum distance included to 3 km. This was due to low data availability at the opposite bank of the fjord due to the presence of sloped terrain and vegetation blocking the lidar's beam.

Using the filtered dataset, each scan was projected from radial dimensions (azimuth, range) to Cartesian coordinates (x, y) on a 10 m resolution meshgrid, and filled using nearest-neighbor interpolation. This approach was chosen to allow the use of standard loss functions, instead of needing to redefine spherical implementations for training the model. As a side effect, this step also increases the magnitude of the data represented in memory.

The 2-D lidar scan images were then scaled to values between zero and one. This acts to normalize the feature range of the scans when input to the neural network. A custom method was applied which prevents outliers from significantly affecting the scaling of the data. First, the mean, minimum and standard deviation across both dimensions were calculated. Next, the maximum values were determined as four standard deviations above the mean (Eq. 1). The scaling was then applied following Eq. 2. Any values above four standard deviations over the mean were then set to one. An example of a processed scan is given in Fig. 4. Note that the scaling range was determined for each scan independently, and therefore does not use any past or future information.

$$X_{\max} = \bar{X} + 4\sigma_X^2 \quad (1)$$

$$X_{scaled} = \frac{X - X_{\min}}{X_{\max} - X_{\min}} \quad (2)$$

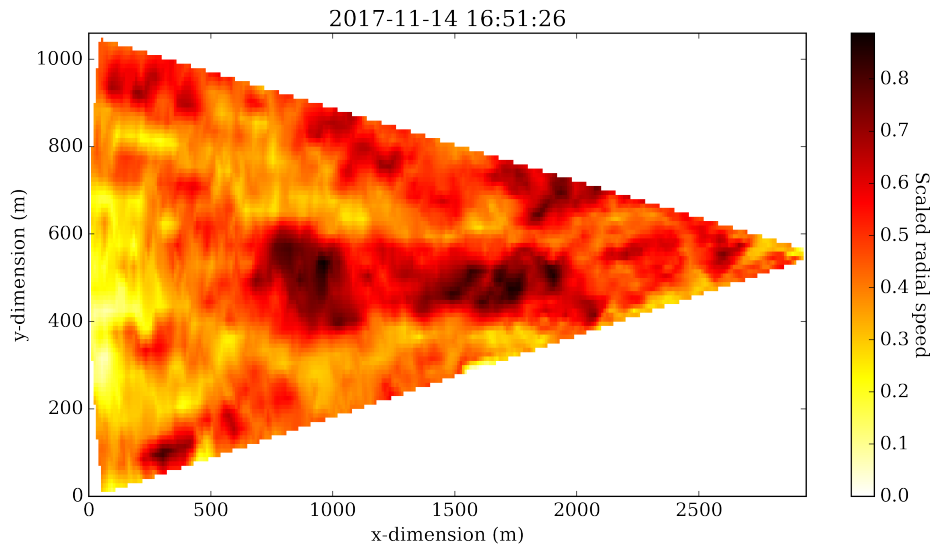


Figure 4. Example of processed scan image from a Sirocco PPI scan

To construct the data structure used for model training, processed scan images over the past input lag length at each scan-time were copied to a new dimension of the array. This represents the inputs fed to the forecasting model as each prediction and subsequent updated fit is made. The number of samples was then reduced at the beginning by the number of input lags, and at the end by the number of samples forecasted to remove periods with partial data on this axis. The final dataset structure is 5 5-dimensional with the shape (time, lags, x dimensions, y dimensions, channels), with radial speed being the only channel.

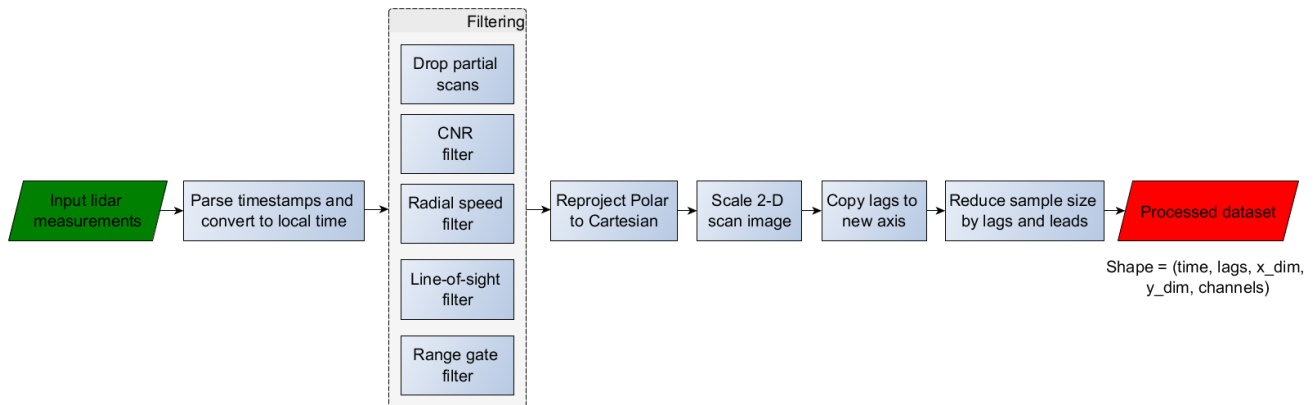


Figure 5. Flowchart of data processing for rooftop lidar (Sirocco)

3.3.2 Brise unit (DBS scans)

A flowchart overview of the data processing steps for Brise is presented in Fig. 6.

Processing of the DBS scans from Brise began similarly to Sirocco, with reading in the lidar measurements, parsing timestamps and removing partial scans at the boundary between scenario files. The same CNR filter thresholds as before were used to filter

5 out observations with low signal quality or hard target contamination. Next, quality checks were performed which ensured that the beam positions were separated by index multiples of 5 (corresponding to the scan strategy outlined in Section 3.2.3).

The wind field reconstruction procedure was performed for all range gates following Section 3.4, and the lowest available height was chosen (50 m AGL). This corresponds to 42.2 m above the position of Sirocco. The reconstruction results in a sampling rate equal to the lidar's LOS measurement speed, which was downsampled to match that of Sirocco (i.e. 13-second
10 averaging).

Horizontal wind components u and v were used to compile the data structure for the reference measurement used in training the model and evaluating forecast errors.

Any undefined values as a result of filtering steps were set to zero. The forecast lead times were also copied to a new timestep axis. The same procedure was followed to reduce the number of samples at the beginning by the number of past lags and at the
15 end by the length of the prediction interval. The final dataset structure is 3-dimensional with the shape (time, forecast leads, channels), where the two channels are reconstructed u and v components from the DBS measurements.

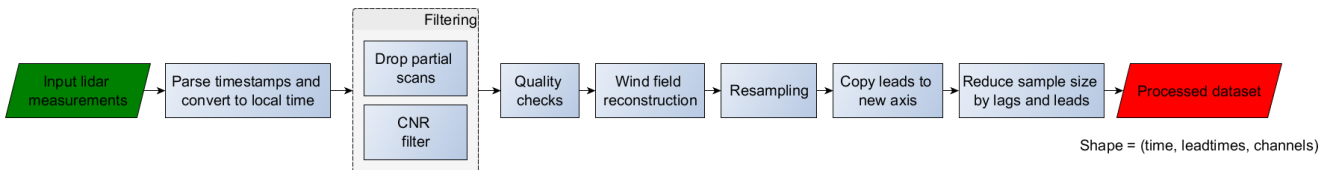


Figure 6. Flowchart of data processing for ground based lidar (Brise)

3.4 Wind field reconstruction (DBS measurements)

A flowchart of the DBS wind field reconstruction process is presented in Fig. 7. To perform the vertical profiling wind field reconstruction with the highest temporal resolution, a sliding window function is needed, which uses the latest available beam
20 measurement to calculate the corresponding value at each timestep. The u and v horizontal wind components are each calculated from two orthogonal beam measurements, while w in this case is directly measured by the vertical beam. It is also possible to independently calculate w from the four orthogonal beams, as is done in the traditional four beam DBS configuration.

When implementing the reconstruction process, a vectorized approach was used. This avoids iterating through the entire dataset and results in a major computational speed advantage. The five line-of-sight (LOS) beams were split up accordingly by their azimuth and elevation angles. Quality controls were then performed to ensure that the beam index positions were separated by the correct LOS separation. Next, the measurements were interleaved along a new dimension according to the corresponding beam-pairs. Finally, the reconstruction equations were applied across the entire dataset at once for each range gate.

$$u = \frac{U_{r_{west}} - U_{r_{east}}}{2 \sin \phi} \quad (3)$$

$$v = \frac{U_{r_{north}} - U_{r_{south}}}{2 \sin \phi} \quad (4)$$

$$w = U_{r_{vertical}} \quad (5)$$

$$w_{calc} = \frac{U_{r_{north}} + U_{r_{south}} + U_{r_{east}} + U_{r_{west}}}{4 \cos \phi} \quad (6)$$

$$10 \quad U_h = \sqrt{u^2 + v^2} \quad (7)$$

$$\psi = \arctan 2(v, u) + c \quad (8)$$

where U_r are the radial speed measurements, φ is the half cone angle, U_h is the scalar horizontal wind speed, ψ is the wind direction, and c represents a potential wind direction offset due to the lidar's orientation.

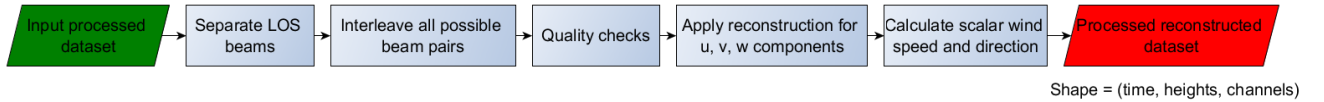


Figure 7. Flowchart of DBS wind field reconstruction from Brise

4 Forecasting methodology

15 4.1 Model training and prediction

4.1.1 Metrics

To evaluate performance of the forecast methods, the root-mean-square error (RMSE) between the predictions and reference values is used. This provides a single measure of predictive skill which penalizes larger errors relative to smaller ones. The RMSE metric is therefore sensitive to outliers which represent the largest potential impacts to the power grid and energy

markets.

$$RMSE = \sum_{i=1}^n \frac{(\hat{y}_i - y_i)^2}{n} \quad (9)$$

The predicted horizontal wind components u and v are similarly transformed to scalar wind speed and direction values using Eq. 7 and 8 for the purposes of the error analysis.

5 4.1.2 Forecast model implementation details

The lidar based forecast model utilizes the Keras framework in Python with Tensorflow backend. Training has taken place on a Google Cloud Compute instance equipped with one NVIDIA Tesla P100 GPU (graphics processing unit). The computation time for processing each batch (i.e. 13-second sample) is 32 ms, which is well within the time constraints for operational use. An overview of the training and prediction process is outlined in Fig. 8.

- 10 A walk-forward testing strategy was used, which emulates online learning of the model during real-time operation. This allows the model to be constantly updated with the latest available data when making out-of-sample predictions, as the samples are highly correlated in time. Therefore, the input layer has a batch size of one. The inputs are processed and scaled PPI images from Sirocco (i.e. rolling 5-minute window of upwind lidar observations), which are used to predict the u and v vector components reconstructed from DBS measurements by Brise across the 5-minute interval which follows.
- 15 Progressing chronologically through the dataset, each sample results in an updated model fit, and a forecast generated spanning 13-seconds to 5-minutes ahead. Subsequently, the dataset walks forward and the latest observations are assimilated resulting in an updated model and a new forecast. As properties of the target data would not be known ahead of time, it is necessary to perform feature scaling of the target signal (i.e. Brise reconstructed wind components) at every step using in-sample observations. This is achieved using Scikit-learn's MinMaxScaler (Scikit-learn (2018)) to match the feature space of the processed PPI
- 20 scan images. This step is not applicable to Sirocco as the scaling has been applied across the image dimensions instead of time (Section 3.3.1).

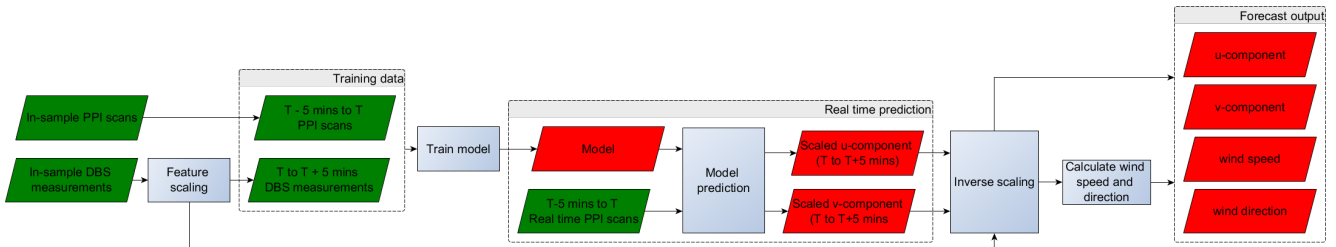


Figure 8. Flowchart of ANN-lidar forecast model operation

The neural network architecture is shown in Fig. 9. It is comprised of two sets of 2D convolutional LSTM layers (Tensorflow (2018)) which are downsampled using 2D MaxPooling (Keras (2018b)) layers before being flattened and then shaped using a fully connected (Dense) layer. Both ConvLSTM2D layers use ReLU (rectified linear unit) activation and neither dropout nor recurrent dropout was applied. As there are multiple stacked recurrent layers, it was necessary to return the entire hidden state output for each timestep so that the dimensionality for the next layer's input sequence is correct. In addition, the LSTM layers are stateful, meaning that the computed hidden states can be propagated between training batches. To preserve the time dimension of the multi-output model, TimeDistributed wrappers (Keras (2018a)) were applied to the non-recurrent layers. The model was compiled using the Adam optimizer (Kingma and Ba (2014)) and mean-squared-error (MSE) loss function. The model was then trained using the walk forward approach previously described, with one fitting epoch (training iteration) per batch (sample), and the model's internal states being reset following each epoch.



Figure 9. ANN-lidar model architecture

Following each forecast, the predicted values are inverse transformed into their (non-scaled) feature space for evaluation against the reference values.

4.1.3 Benchmarking (Persistence and ARIMA)

Two forecasting strategies based on standard methods applied within this timescale were carried out in order to benchmark the relative skill of the more neural network approach. These benchmark methods rely only on the univariate target signal, without any of the forward-looking information provided by the rooftop lidar (Sirocco). Scalar quantities of wind speed and direction are used in both cases. These are derived from the reconstructed horizontal winds of the DBS lidar (Brise) as outlined in Section 3.3.2.

The first benchmark is the persistence method, which forecasts future values to be the same as the most recent observation.

$$20 \quad \hat{y}_{t+\Delta t} = y_t \quad (10)$$

where y is the reference signal and Δt is the forecast horizon.

The second benchmark is a time series modelling approach called ARIMA (autoregressive integrated moving average). This method utilizes past lags (AR) of the target variable and a moving average model (MA), along with differencing (I) of the series to transform it to a stationary process. Stationarity is determined through unit root testing, typically using the augmented Dickey–Fuller test. Seasonal adjustment here is not necessary, but would need to be applied for longer time series. The model

parameters ARIMA (p, d, q) represent the number of lags (p), the degree of differencing (d), and the order of the moving average model (q). The p parameter is determined through inspection of the autocorrelation function (ACF) and partial autocorrelation function (PACF), with consideration to increased computational demand for increasing number of lags (Fig. 10). The ACF describes the linear dependence of the signal with itself over a range of past values, while the PACF excludes the effects (indirect correlations) of intermediary lags. The d parameter is determined by performing an increasing number of differencing steps until the series becomes stationary (where the mean, variance, and probability distribution does not change with time). The final (q) (MA) component represents a weighted moving average of the past q error steps (exponential smoothing).

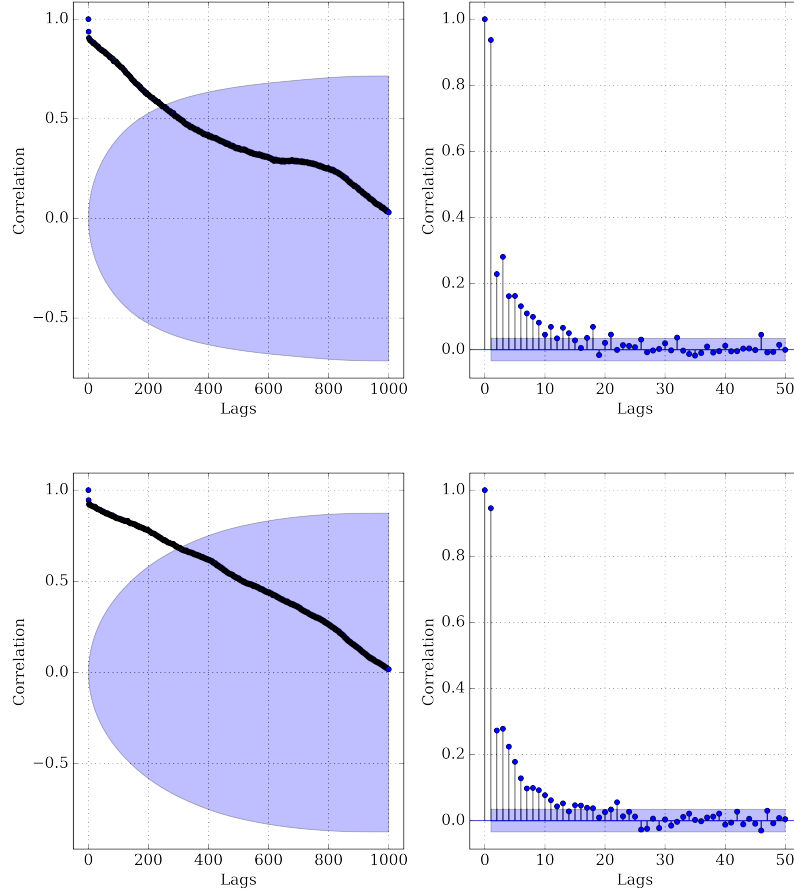


Figure 10. ACF (left) and PACF (right) plots (top: wind speed, bottom: wind direction) beginning from lag zero. The area outside the shaded region represents the 95% confidence interval where the correlation is non-zero (i.e. strong serial correlation)

The non-seasonal ARIMA formulation can be written as:

$$\hat{y}'_t = c + \phi_1 y'_{t-1} + \cdots + \phi_p y'_{t-p} + \theta_1 \varepsilon_{t-1} + \cdots + \theta_q \varepsilon_{t-q} + \varepsilon_t + c \quad (11)$$

Where y' is the arbitrarily d-differenced series, θ are parameters of the AR model, and ϵ are white noise error terms.

The ARIMA forecasts were generated in the same manner as the walk-forward training and prediction approach outlined in Section 4.1.2. The model was incrementally fit using in-sample data and predictions were made at each time step in a multi-output setup across the entire forecast length (i.e. every 13 s from 1 to 23 steps (5 minutes) ahead).

- 5 Two model formulations were tested, separately for wind speed and wind direction. Benchmark #1 is of order (5,1,0) which neglects the MA component and becomes a differenced fifth order AR model. Benchmark #2 is an ARIMA model of order (5,1,1). The parameters were fit using conditional sum-of-squares likelihood maximization.

Note that the wind direction signal over the time period chosen does not approach the boundary between 0 and 360 degrees, so it is not necessary to consider this when calculating the errors.

10 5 Results

5.1 Validation of wind field reconstruction method

To demonstrate the correct processing of the DBS measurements from Brise (according to Section 3.4), a validation has been included which compares the lidar obtained wind field to that measured at the nearby met-mast described in Section 3.2.4. The met-mast observations have been downsampled to match the sampling rate of the lidar. The data points have a time resolution
15 of 13-seconds and the sample size is 3220 observations.

The comparisons show generally good agreement between both independent instruments considering their spatial separation. The lidar reconstructed wind speeds from Brise indicate a small positive bias which increases with wind speed. The wind direction however is slightly underestimated relative to the met-mast. Nevertheless, the results confirm that there are no serious flaws in the source data or reconstruction methods.

20 5.2 2D correlation of PPI scans

A core assumption of the forecast model is that spatial patterns in the lidar scans are trackable as they advect downwind. An inspection of the cross-correlations between scan pairs has provided insight into this assumption. Six processed PPI scans from Sirocco are shown in Fig. 12, which are spaced in intervals of 3 scan-times (i.e. 40 s between each frame) for compactness. The darker structure with a higher radial speed visibly advects downwind while also transforming its properties due to turbulence.
25 The tail is centered at 2500 m upwind in the first frame, and 300 m in the last frame. This corresponds to an advection speed of 11 m/s, which closely matches the wind speed during the period (11.2 m/s).

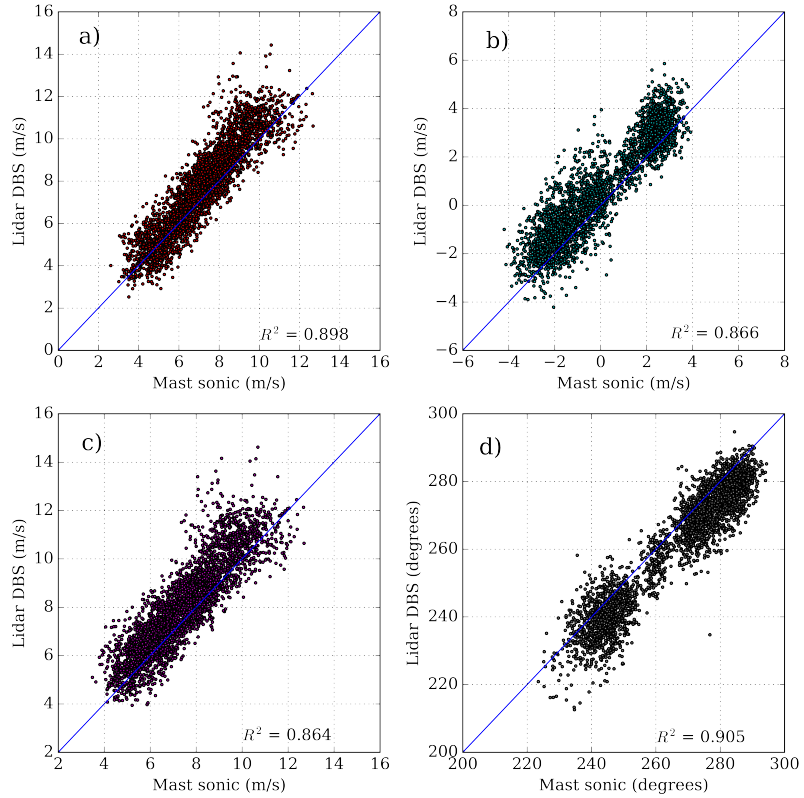


Figure 11. Validation of 50m lidar reconstructed DBS measurements (Brise) against 44m sonic measurements from nearby met-mast. a) u-component, b) v-component, c) wind speed, d) wind direction

Fig. 13 presents a 2D cross correlation result between one base image and the 1st to 8th scans which follow. This indicates the spatial distribution of correlations between the two images. The point where the maximum exists represents similar features appearing in both images. The advection rate of the structure from the correlation method (1km in 104 s = 9.6 m/s) also matches the average wind speed during the period (9.53 m/s). The 2D cross correlation was calculated using a 2D convolution function
 5 with the second image reversed along both axes.

5.3 Forecast results

Overall RMSE comparisons of the three forecast methods are presented in Fig. 14 both for wind speed and wind direction. This compares the RMSE performance by lead time of the various benchmarks together with the Lidar-ANN model.

The Lidar-ANN method outperforms two of the benchmarks (persistence and the integrated AR model) for the first 17 scan-times ahead (0.22-3.68 minutes). Following this and up to the maximum forecast length, the Lidar-ANN skill quickly deteriorates. The ARIMA(5,1,1) benchmark achieves the lowest RMSE across lead times, except for the first two forecast steps (13
 10

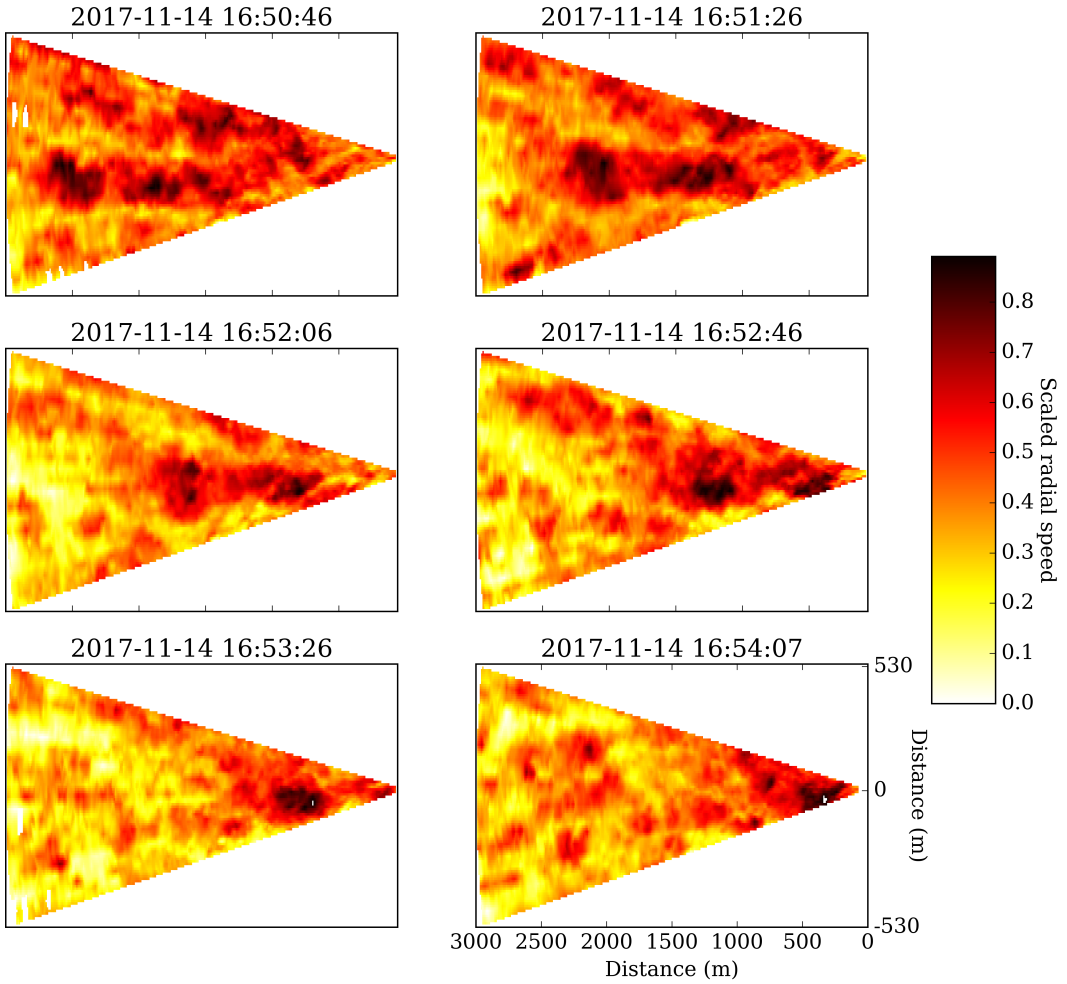


Figure 12. Example of PPI scan sequence (order: top-left to bottom-right) in intervals of 3 scans (i.e. 40 seconds between frames)

s and 26 s). Persistence performs well only at the shortest lead time (13 s ahead). Table 3 indicates the relative RMSE skill of the Lidar-ANN approach compared with the three benchmark methods.

The Lidar-ANN model predictions for the 1.08 minute ahead forecast horizon are shown in Fig. 15 and Fig. 16. Through inspection of the time series, it is clear that the model predictions follow the overall reference signal. However, they do not capture the fine variations (i.e. turbulence). This is shown as scatter around the $y=x$ line in 16.

Lidar-ANN model predictions exhibit larger amounts of scatter at higher wind speeds ($> 10 \text{ m/s}$). The errors are also larger for wind directions where the inflow is not closely aligned with the center of the lidar scan (i.e. far from 270°).

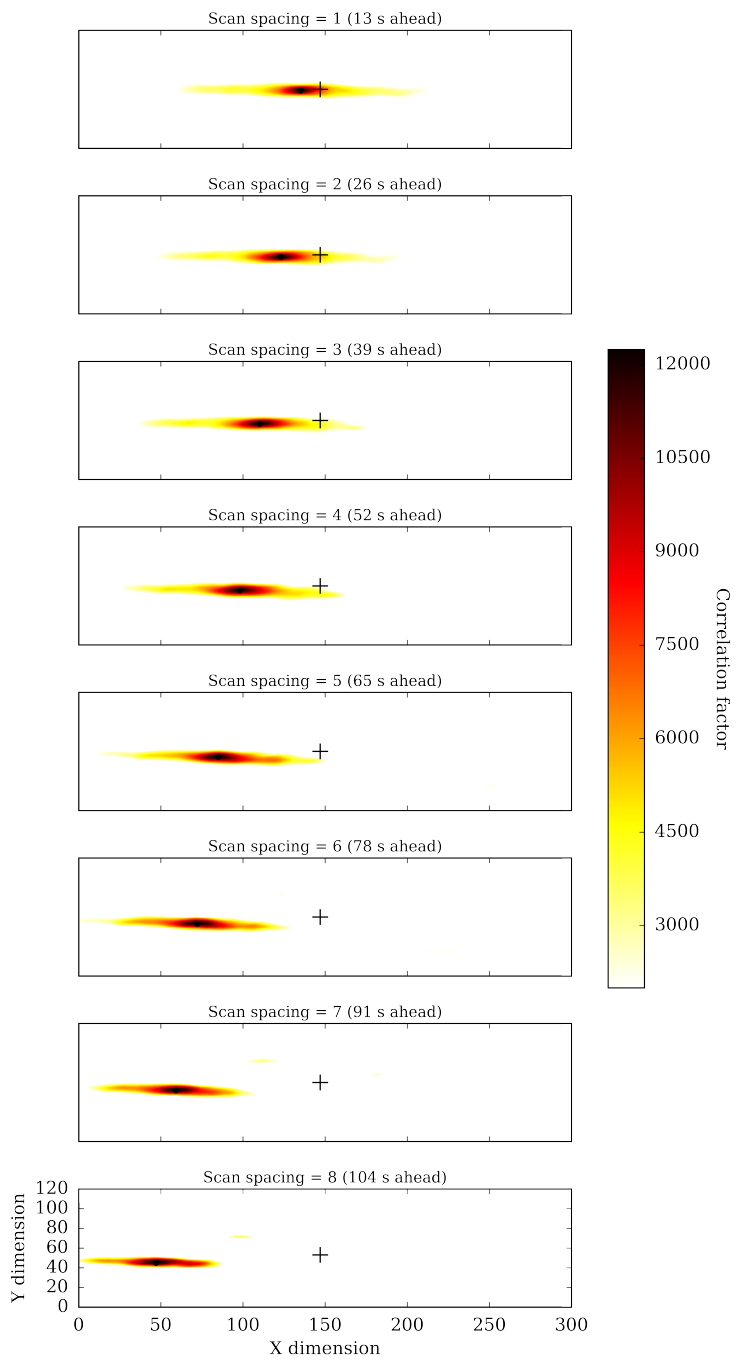


Figure 13. Example case of 2D cross-correlations between a base image and 1 to 8 scan-times (13-104 s) ahead. This period has a wind speed of 9.53 m/s and direction of 284 degrees. The center point of the images is denoted with a plus sign

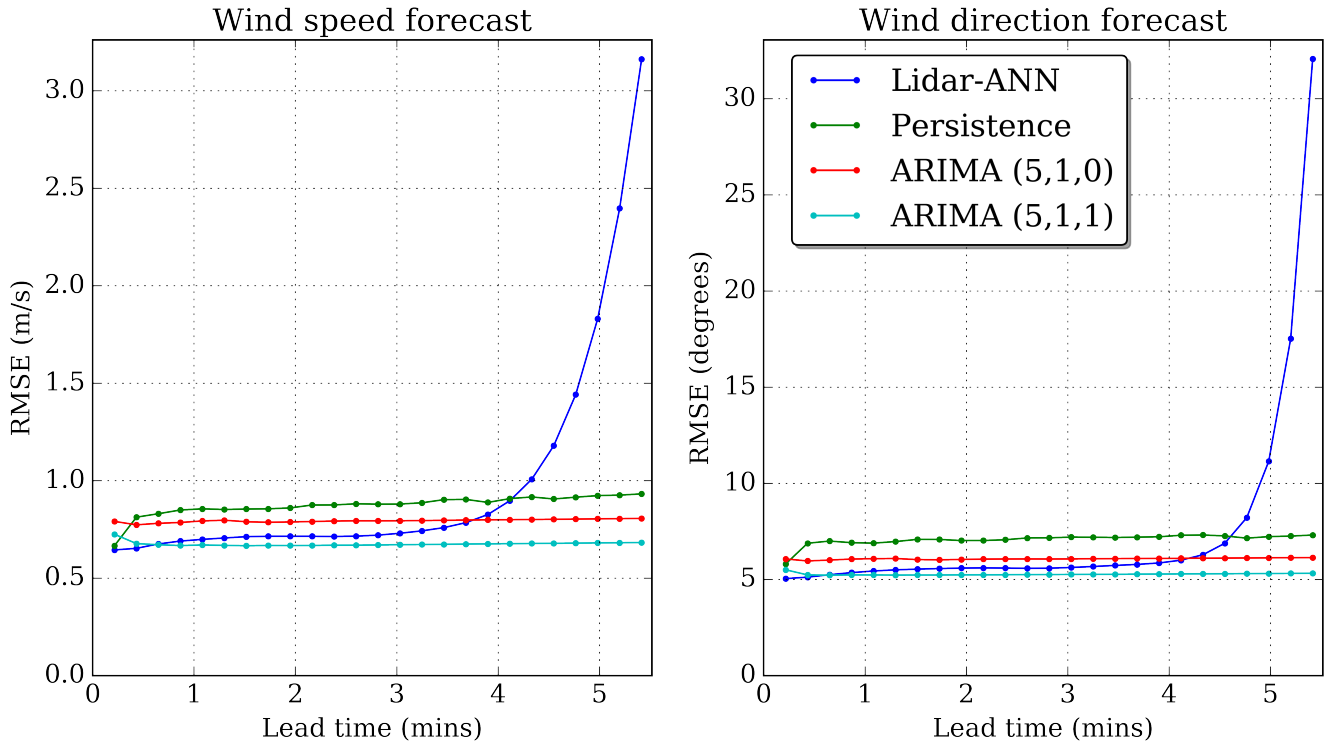


Figure 14. Forecast RMSE by lead time for all methods (left: wind speed, right: wind direction)

6 Discussion

There has been no tuning performed in the way of hyperparameter optimization, and the overall architecture of the model has been inspired from other frame prediction problems in the computer vision field. This suggests that the ANN-lidar model performance could be further improved through such changes, in combination with a sensitivity analysis. Other suitable methods which were explored early during this study but not prioritized include traditional image processing algorithms such as: the Sobel filter for separating gradients in the x and y direction, edge detection approaches including the Canny operator to define and track coherent structures, and dense optical flow methods for calculation the motion between frame pairs (Farnebäck (2003)).

A fact of the lidar PPI scans is that they do differ from the majority of image sources as they are not a snapshot in time, but rather acquired throughout the scanning period. As the scanner head motion sweeps through the scan area, features can be smeared or otherwise distorted. This limitation could be addressed with interpolation between neighboring scans. However, as the effect is largest with structures moving perpendicularly to the beam angle, this issue has been disregarded as the scan rate is fast (13 s) and the wind direction is generally aligned with the beam when measuring inflow.

Table 3. Results comparison of Lidar-ANN model to benchmarks by lead time. Improved skill is colored green while diminished skill is colored red

Lead time (mins)	Relative improvement of Lidar-ANN model compared with:						
	Wind speed			Wind direction			
	Persistence (%)	ARIMA (5,1,0) (%)	ARIMA (5,1,1) (%)	Persistence (%)	ARIMA (5,1,0) (%)	ARIMA (5,1,1) (%)	
0.22	3.30	18.53	11.10	13.09	16.89	8.41	
0.43	19.68	15.60	3.57	25.65	14.15	2.22	
0.65	18.71	13.58	-0.57	25.05	12.71	-0.44	
0.87	18.77	12.16	-3.47	22.56	11.66	-2.29	
1.08	18.35	11.94	-4.26	21.05	10.54	-3.97	
1.30	17.17	11.45	-5.70	21.13	9.70	-5.15	
1.52	16.62	9.71	-6.97	21.88	8.24	-5.86	
1.73	16.50	9.15	-7.07	21.41	7.54	-6.43	
1.95	16.96	9.37	-7.12	20.42	7.45	-6.75	
2.17	18.37	9.61	-7.05	20.28	7.53	-6.90	
2.38	18.51	10.00	-6.67	20.87	7.78	-6.64	
2.60	18.86	9.92	-6.90	22.09	8.04	-6.26	
2.82	18.09	9.26	-7.54	22.05	7.88	-6.29	
3.03	17.04	8.08	-8.73	21.97	7.35	-6.91	
3.25	16.26	6.64	-10.45	21.18	6.64	-7.77	
3.47	15.91	4.70	-12.75	20.27	5.85	-8.75	
3.68	13.21	1.67	-16.27	19.73	5.07	-9.61	
3.90	7.00	-3.43	-22.32	18.89	3.91	-10.93	
4.12	1.20	-12.17	-32.62	17.80	1.61	-13.53	
4.33	-9.94	-25.84	-48.69	14.10	-2.89	-18.77	
4.55	-30.19	-47.14	-73.88	5.25	-12.62	-29.98	
4.77	-57.58	-79.64	-112.31	-14.97	-34.33	-55.07	
4.98	-98.38	-127.87	-169.25	-54.31	-82.12	-110.15	

A necessary point of mention is that current commercial scanning lidar systems are expensive to purchase, require skilled technical staff to operate and maintain, and do not always provide sufficient signal across the entire measurement range. Therefore the added value must be large enough to justify its use. As shown in this and other minute-scale wind prediction studies, the “free” statistical approaches which utilize only historical data from existing instruments perform well on these time scales. However it is necessary to both have access to and store the high-frequency measurements for building and testing statistical time series models like ARIMA. This is highly suggested for operators who have an interest in improving their forecast performance.

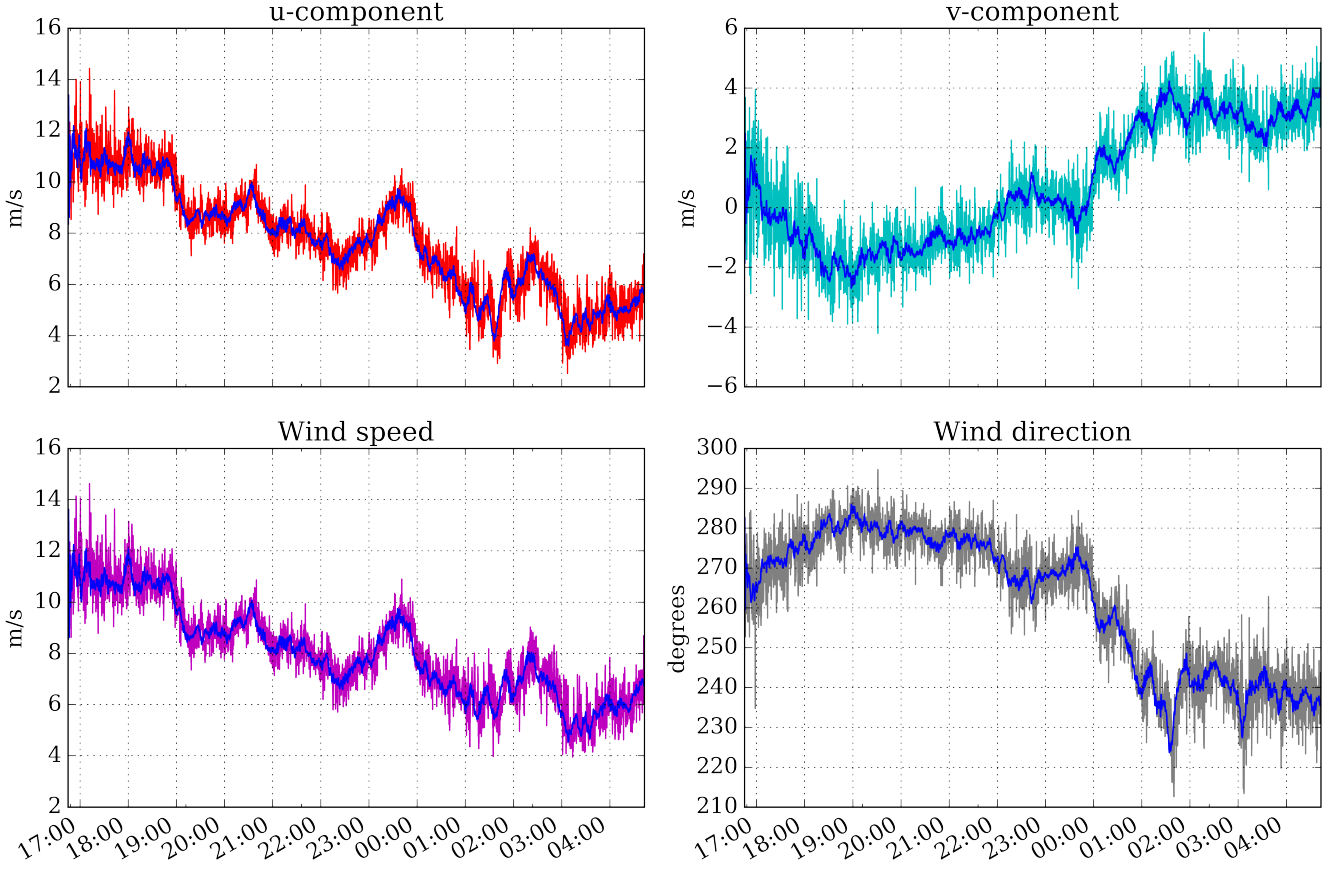


Figure 15. Time series of Lidar-ANN forecast (blue) with DBS reference signals at the 1.08-minute forecast interval. (top left: u-component, top right: v-component, bottom left: wind speed, bottom right: wind direction)

7 Conclusions

This study has demonstrated a groundwork introduction for utilizing ANN methods together with 2D upwind lidar scans for the purpose of minute-scale wind forecasting. The field experiment has successfully provided detailed measurements of the site inflow at large distances (3 km effective) upstream, together with high resolution wind profiles which constitute the downstream reference.

Coherent wind structures present in the horizontal PPI scans from the rooftop scanning lidar have been shown to correlate strongly with scans taken in the range of up to 5-minutes apart. This enables the tracking of spatiotemporal features present in the scans on very-short timescales. A recently developed convolutional recurrent neural network cell (ConvLSTM) has been identified as appropriate for modelling the complex space-time relationships present in the scan image sequences. An ANN

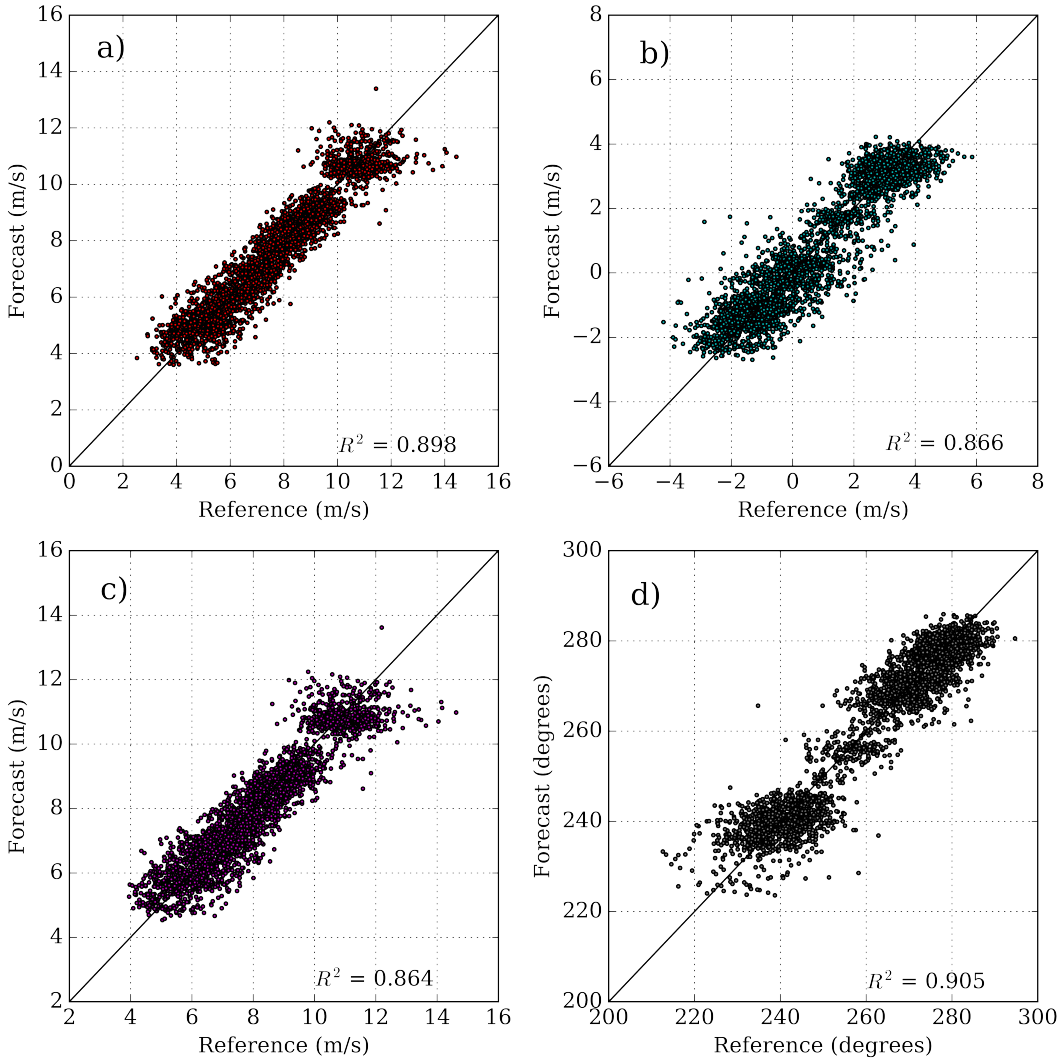


Figure 16. Scatterplot comparison between Lidar-ANN forecast and DBS references for the 1.08-minute forecast interval for: a) u-component, b) v-component, c) wind speed, d) wind direction

approach consisting of these cells and inspired by video frame prediction engines has been applied to create an online learning forecast model. The model inputs at each timestep consist of the past 5-minutes of upwind lidar scans, which are used to predict the horizontal wind vector at the downwind reference position with a forecast horizon spanning 13-seconds to 5-minutes ahead. The model has been designed to emulate real-time operation, and when utilizing hardware optimized for ANN operations (i.e. 5 a GPU or AISC), the model is fully capable of producing forecasts which are usable for real-time decision making.

The horizontal wind vector components (u and v) have been utilized as the predictand in order to enable forecasts of both wind speed and direction. This allows for better integration into wind farm controllers and power curve models.

The ANN-lidar model has demonstrated a high degree of skill for predictions up to 4-minutes ahead. When comparing performance with other standard benchmarks, the ANN-lidar method outperforms persistence as well as the integrated AR model. However, the ARIMA benchmark has shown remarkable skill in achieving a lower RMSE than the ANN-lidar method following after the first two timesteps (i.e. from 39 s onwards). This signifies the challenge of demonstrating value with complex
5 approaches over time series modelling which use already available historical data. Nevertheless, model refinements and tuning are recommended, in conjunction with training on a larger dataset to explore further prospects of the approach.

Data availability. The measurement data used in this study is publicly available under the CC BY 4.0 license. The dataset is available in Simon and Lea (2019)

Author contributions. E.S. conducted the research work, performed all data analysis, and composed the manuscript. E.S. designed the field
10 experiment and conducted it together with Guillaume Lea. M.C. supervised the overall research work and made contributions to the scientific direction. All co-authors participated in discussing and revising the paper.

Competing interests. The authors declare that they have no conflicts of interest.

Acknowledgements. Guillaume Lea is recognized for his work in organizing and conducting the field campaign. Sue Ellen Haupt, David John Gagne II and the RAL group at NCAR are thanked for hosting the research stay where this study was conducted and for providing excellent
15 mentorship. Tobias Ahsbahs is thanked for his assistance with the vectorized DBS reconstruction code. Google is also acknowledged for providing free usage credits on their Cloud Compute platform.

References

- Ahsbahs, T., Badger, M., Karagali, I., and Larsén, X. G.: Validation of Sentinel-1A SAR Coastal Wind Speeds Against Scanning LiDAR, *Remote Sensing*, 9, 552, <https://doi.org/10.3390/rs9060552>, <https://www.mdpi.com/2072-4292/9/6/552>, 2017.
- Brower, M., ed.: *Wind resource assessment: a practical guide to developing a wind project*, Wiley, Hoboken, N.J, 2012.
- 5 Cariou, J.-P., Augere, B., and Valla, M.: Laser source requirements for coherent lidars based on fiber technology, *Comptes Rendus Physique*, 7, 213–223, <https://doi.org/10.1016/j.crhy.2006.03.012>, <http://www.sciencedirect.com/science/article/pii/S1631070506000818>, 2006.
- Carpenter, R. L.: Short-term Numerical Forecasts Using WindTracer Lidar Data, *AMS*, <https://ams.confex.com/ams/93Annual/webprogram/Paper216094.html>, 2013.
- EPEX SPOT: Intraday Lead Time, http://www.epexspot.com/en/product-info/intradaycontinuous/intraday_lead_time, 2019.
- 10 Farnebäck, G.: Two-Frame Motion Estimation Based on Polynomial Expansion, in: *Image Analysis*, edited by Bigun, J., Gustavsson, T., Goos, G., Hartmanis, J., and van Leeuwen, J., vol. 2749, pp. 363–370, Springer Berlin Heidelberg, Berlin, Heidelberg, https://doi.org/10.1007/3-540-45103-X_50, http://link.springer.com/10.1007/3-540-45103-X_50, 2003.
- Giebel, G., Brownsword, R., Kariniotakis, G., Denhard, M., and Draxl, C.: The State-Of-The-Art in Short-Term Prediction of Wind Power, *ANEMOS.plus*, <https://doi.org/10.11581/DTU:00000017>, <https://doi.org/10.11581/DTU:00000017>, 2011.
- 15 Goodfellow, I., Bengio, Y., and Courville, A.: *Deep Learning*, MIT Press, 2016.
- Google Developers: Machine Learning Crash Course, <https://developers.google.com/machine-learning/crash-course/>, 2019.
- Greff, K., Srivastava, R. K., Koutník, J., Steunebrink, B. R., and Schmidhuber, J.: LSTM: A Search Space Odyssey, *IEEE Transactions on Neural Networks and Learning Systems*, 28, 2222–2232, <https://doi.org/10.1109/TNNLS.2016.2582924>, <http://arxiv.org/abs/1503.04069>, arXiv: 1503.04069, 2017.
- 20 Halo Photonics: Stream Line Doppler Lidar systems, http://www.halo-photonics.com/StreamLine-XR-Doppler_Lidar.htm, 2018.
- Hochreiter, S. and Schmidhuber, J.: Long Short-Term Memory, *Neural Computation*, 9, 1735–1780, <https://doi.org/10.1162/neco.1997.9.8.1735>, <https://www.mitpressjournals.org/doi/10.1162/neco.1997.9.8.1735>, 1997.
- Keras: Layer wrappers, <https://keras.io/layers/wrappers/>, 2018a.
- Keras: Pooling Layers, <https://keras.io/layers/pooling/>, 2018b.
- 25 Kim, Y.: Convolutional Neural Networks for Sentence Classification, arXiv:1408.5882 [cs], <http://arxiv.org/abs/1408.5882>, arXiv: 1408.5882, 2014.
- Kingma, D. P. and Ba, J.: Adam: A Method for Stochastic Optimization, arXiv:1412.6980 [cs], <http://arxiv.org/abs/1412.6980>, arXiv: 1412.6980, 2014.
- Laptev, N., Yosinski, J., Li, L. E., and Smyl, S.: Time-series extreme event forecasting with neural networks at uber, in: *International Conference on Machine Learning*, pp. 1–5, http://www.cs.columbia.edu/~lierranli/publications/TSW2017_paper.pdf, 2017.
- 30 Leica Geosystems: Leica Viva GNSS GS15 receiver Datasheet, https://w3.leica-geosystems.com/downloads123/zz/gpsgis/viva%20gnss/brochures-datasheet/leica_viva_gnss_gs15_receiver_ds_en.pdf, 2012.
- Leosphere: Scanning Windcube, <https://www.leosphere.com/products/scanning-wincube/>, 2018.
- Li, F.-F.: CS231n: Convolutional Neural Networks for Visual Recognition, <http://cs231n.stanford.edu/>, 2018.
- 35 Liang, X.: An Integrating Velocity–Azimuth Process Single-Doppler Radar Wind Retrieval Method, *Journal of Atmospheric and Oceanic Technology*, 24, 658–665, <https://doi.org/10.1175/JTECH2047.1>, <https://journals.ametsoc.org/doi/abs/10.1175/JTECH2047.1>, 2007.

- Magerman, B.: Short-Term Wind Power Forecasts using Doppler Lidar, Ph.D. Thesis, <http://adsabs.harvard.edu/abs/2014PhDT.....314M>, 2014.
- Mahoney, W. P., Parks, K., Wiener, G., Liu, Y., Myers, W. L., Sun, J., Monache, L. D., Hopson, T., Johnson, D., and Haupt, S. E.: A Wind Power Forecasting System to Optimize Grid Integration, *IEEE Transactions on Sustainable Energy*, 3, 670–682, 5 <https://doi.org/10.1109/TSTE.2012.2201758>, 2012.
- Mann, J., Menke, R., Vasiljević, N., Berg, J., and Troldborg, N.: Challenges in using scanning lidars to estimate wind resources in complex terrain, *Journal of Physics: Conference Series*, 1037, 072017, <https://doi.org/10.1088/1742-6596/1037/7/072017>, <http://stacks.iop.org/1742-6596/1037/i=7/a=072017>, 2018.
- Mislan, D. B. and Streich, P.: To the Sea! Sealand and Other Wannabe States, in: *Weird IR: Deviant Cases in International Relations*, 10 edited by Mislan, D. B. and Streich, P., pp. 15–28, Springer International Publishing, Cham, https://doi.org/10.1007/978-3-319-75556-4_2, 2019.
- Mitsubishi Electric: Ground based Long-range Doppler Lidar, <http://www.mitsubishielectric.com/bu/lidar/products/coherent/index.html>, 2018.
- Moehrlen, C.: Uncertainty in wind energy forecasting, <https://cora.ucc.ie/handle/10468/193>, 2004.
- Ogunmolu, O., Gu, X., Jiang, S., and Gans, N.: Nonlinear Systems Identification Using Deep Dynamic Neural Networks, arXiv:1610.01439 15 [cs], <http://arxiv.org/abs/1610.01439>, arXiv: 1610.01439, 2016.
- Schlipf, D., Schlipf, D. J., and Kühn, M.: Nonlinear model predictive control of wind turbines using LIDAR, *Wind Energy*, 16, 1107–1129, <https://doi.org/10.1002/we.1533>, <https://onlinelibrary.wiley.com/doi/abs/10.1002/we.1533>, 2012.
- Scikit-learn: sklearn.preprocessing.MinMaxScaler, <https://scikit-learn.org/stable/modules/generated/sklearn.preprocessing.MinMaxScaler.html>, 2018.
- Shi, X., Chen, Z., Wang, H., Yeung, D.-Y., Wong, W.-k., and Woo, W.-c.: Convolutional LSTM Network: A Machine Learning Approach for Precipitation Nowcasting, arXiv:1506.04214 [cs], <http://arxiv.org/abs/1506.04214>, arXiv: 1506.04214, 2015.
- Simon, E. and Lea, G.: LASCAR Experiment Dataset, <https://doi.org/10.11583/DTU.7321070>, 2019.
- Simon, E., Courtney, M., and Vasiljevic, N.: Minute-Scale Wind Speed Forecasting Using Scanning Lidar Inflow Measurements, *Wind 25 Energy Science Discussions*, 2018, 1–30, <https://doi.org/10.5194/wes-2018-71>, <https://www.wind-energ-sci-discuss.net/wes-2018-71/>, 2018.
- Strauch, R. G., Weber, B. L., Frisch, A. S., Little, C. G., Merritt, D. A., Moran, K. P., and Welsh, D. C.: The Precision and Relative Accuracy of Profiler Wind Measurements, *Journal of Atmospheric and Oceanic Technology*, 4, 563–571, [https://doi.org/10.1175/1520-0426\(1987\)004<0563:TPARAO>2.0.CO;2](https://doi.org/10.1175/1520-0426(1987)004<0563:TPARAO>2.0.CO;2), <https://journals.ametsoc.org/doi/10.1175/1520-0426%281987%3004%3C0563%3ATPARAO%3E2.0.CO%3B2>, 1987.
- Taigman, Y., Yang, M., Ranzato, M., and Wolf, L.: DeepFace: Closing the Gap to Human-Level Performance in Face Verification, pp. 1701–1708, https://www.cv-foundation.org/openaccess/content_cvpr_2014/html/Taigman_DeepFace_Closing_the_2014_CVPR_paper.html, 2014.
- Tensorflow: tf.keras.layers.ConvLSTM2D, https://www.tensorflow.org/api_docs/python/tf/keras/layers/ConvLSTM2D, 2018.
- Valdecabres, L., Peña, A., Courtney, M., Bremen, L. v., and Kühn, M.: Very short-term forecast of near-coastal flow using scanning lidars, 35 *Wind Energy Science Discussions*, pp. 1–22, <https://doi.org/https://doi.org/10.5194/wes-2017-48>, <https://www.wind-energ-sci-discuss.net/wes-2017-48/>, 2017.

- Valldcabres, L., Nygaard, N., Vera-Tudela, L., von Bremen, L., Kühn, M., Valldcabres, L., Nygaard, N. G., Vera-Tudela, L., von Bremen, L., and Kühn, M.: On the Use of Dual-Doppler Radar Measurements for Very Short-Term Wind Power Forecasts, *Remote Sensing*, 10, 1701, <https://doi.org/10.3390/rs10111701>, <https://www.mdpi.com/2072-4292/10/11/1701>, 2018.
- Vasiljevic, N., Lea, G., Courtney, M., Cariou, J.-P., Mann, J., and Mikkelsen, T.: Long-Range WindScanner System, *Remote Sensing*, 8, 896, 5 <https://doi.org/10.3390/rs8110896>, <https://www.mdpi.com/2072-4292/8/11/896>, 2016.
- Veiga Rodrigues, C., Palma, J., Vasiljevic, N., Courtney, M., and Mann, J.: Coupled simulations and comparison with multi-lidar measurements of the wind flow over a double-ridge, *Journal of Physics: Conference Series (Online)*, 753, <https://doi.org/10.1088/1742-6596/753/3/032025>, 2016.
- Vollmer, L., Dooren, M. v., Trabucchi, D., Schneemann, J., Steinfeld, G., Witha, B., Trujillo, J., and Kühn, M.: First comparison of LES of 10 an offshore wind turbine wake with dual-Doppler lidar measurements in a German offshore wind farm, *Journal of Physics: Conference Series*, 625, 012 001, <https://doi.org/10.1088/1742-6596/625/1/012001>, <http://stacks.iop.org/1742-6596/625/i=1/a=012001>, 2015.
- Wagner, R., Pedersen, T. F., Courtney, M., Antoniou, I., Davoust, S., and Rivera, R. L.: Power curve measurement with a nacelle mounted lidar, *Wind Energy*, 17, 1441–1453, <https://doi.org/10.1002/we.1643>, <https://onlinelibrary.wiley.com/doi/abs/10.1002/we.1643>, 2014.